Annual Growth Rates of Column-Averaged CO_2 Inferred from Total Carbon Column Observing Network (TCCON)

Nasrin Mostafavi Pak[1], Jonas Hachmeister[2], Markus Rettinger[1], Matthias Buschmann[2], Nicholas M. Deutscher[3], David W.T. Griffith[3], Laura T. Iraci[4], Xin Lan[5, 6], Erin McGee[7], Isamu Morino[8], Dave Pollard[9], Coleen M. Roehl[10], Kimberly Strong[7], Rigel Kivi[11], and Paul Wennberg[10]

[1]Karlsruhe Institute of Technology (KIT/IMK-IFU), Garmisch-Partenkirchen, Germany
[2]Institute of Environmental Physics, University of Bremen, Bremen, Germany
[3]Environmental Futures Research Institute and School of Science, University of Wollongong, Wollongong, NSW, Australia
[4]NASA Ames Research Center, Mountain View, CA, USA
[5]Cooperative Institute for Research In Environmental Sciences, University of Colorado Boulder, USA
[6]Global Monitoring Laboratory, National Oceanic and Atmospheric Administration (NOAA), USA
[7]Department of Physics, University of Toronto, Toronto, Ontario, Canada
[8]Earth System Division, National Institute for Environmental Studies (NIES), Japan
[9]New Zealand Institute for Earth Science Limited, Lauder, New Zealand
[10]California Institute of Technology, Pasadena, CA, USA
[11]Finnish Meteorological Institute, Sodankylä, Finland

Correspondence: Nasrin Mostafavi Pak (seyedehnasrin.mostafavipak@kit.edu)

Abstract.

Monitoring annual atmospheric CO_2 growth rates is a key constraint on assessing the long-term effectiveness of emission reduction strategies. We analyzed annual growth rates of column-averaged dry-air mole fractions of CO_2 (XCO_2) using long-term data from 12 sites within the Total Carbon Column Observing Network (TCCON), spanning four regions: the Arctic, two

5   Northern Hemisphere midlatitude bands (40–50° N and 30–40° N), and the Southern Hemisphere. While in situ ground-based measurements provide detailed records of near-surface CO_2 concentrations, XCO_2 reflects the column-averaged abundance across the entire atmosphere, offering a complementary perspective.

We compared TCCON-derived growth rates with ground-based in situ observations from the Mauna Loa Observatory (MLO). Three calculation methods—Monthly Mean (MM), Fourier Fit residuals (FF), and Dynamic Linear Model (DLM)—were

10   evaluated, with particular attention to the Eureka site, where polar night introduces substantial data gaps. In addition, the Copernicus Atmosphere Monitoring Service (CAMS) reanalysis product was used to assess consistency with TCCON-based growth rates and to evaluate each method's robustness to missing data. Among the methods tested, the DLM approach proved most resilient to data gaps.

Regionally averaged CO_2 growth rates, calculated from 2010 or from the earliest available data through 2024, ranged from

15   approximately 2.33 to 2.40 ppm/year. The most prominent signal was associated with the 2015–2016 El Niño – Southern Oscillation (ENSO) event, during which growth rates increased by up to 1.7 ppm/year. The impact of COVID-19-related emission reductions in 2020 was also examined: a decline of 0.4 ppm/year was observed in the 30–40°N region, whereas

other regions showed no significant decline. Correlation analysis between growth rates and ENSO strength revealed significant relationships in the Southern Hemisphere and at Mauna Loa, but not in northern mid- or high-latitude regions.

1 Introduction

It is estimated that Earth's global surface temperature were more than 1°C warmer in the decade 2011–2020 compared to pre-industrial levels (Lee et al., 2023). The rise in Earth's surface temperature has severe consequences, including sea level rise, extreme heat events, drastic shifts in precipitation patterns, and droughts, all of which pose significant risks to ecosystems and human societies (Lee et al., 2023). To mitigate these impacts and achieve the goals set by the Paris Agreement, limiting global temperature rise to 1.5°C by 2050, there is an urgent need to drastically reduce anthropogenic greenhouse gas (GHG) emissions and reach net-zero CO_2 emissions (UNFCC, 2015; Lee et al., 2023).

Since the Industrial Revolution, anthropogenic CO_2 emissions have generally monotonically increased, but with occasional declines during major global events, such as the 2008 economic recession and the 2020 COVID-19 pandemic (Crippa et al., 2023). During these periods, economic slowdowns led to temporary reductions in CO_2 emissions. The COVID-19 pandemic, in particular, provides a unique opportunity to evaluate the atmospheric response to an abrupt and large-scale drop in emissions. In 2019, global CO_2 emissions were estimated at 37.8 Gt/year (Crippa et al., 2023). According to IPCC scenarios consistent with limiting warming to 1.5°C, global GHG emissions must decline by approximately 84% by 2050 relative to 2019 levels (Lee et al., 2023), implying steep reductions in gross emissions and/or increased CO_2 removal. This corresponds to an average annual reduction of approximately 1 Gt CO_2/year. Due to restrictions related to the COVID-19 pandemic, global fossil fuel CO_2 emissions in 2020 decreased by approximately 1.9 Gt compared to 2019 (Crippa et al., 2023), a drop nearly twice as large as this expected annual average. Understanding whether such reductions are detectable in atmospheric CO_2 concentrations is crucial for assessing the effectiveness of future emission reduction strategies.

Data from National Oceanic and Atmospheric Administration (NOAA) Global Monitoring Laboratory indicate that the annual CO_2 growth rate, as measured at the Mauna Loa Observatory, decreased by 8% in 2020. However, this reduction is relatively small compared to the much larger increases observed during strong El Niño events, such as the 45% increase in 2015–2016 (NOAA, 2024). This highlights the challenge of distinguishing between natural variability and anthropogenic emission changes. Moreover, monitoring atmospheric CO_2 concentrations across multiple regions is essential, as the detectability of emission-driven changes can vary due to differences in regional fossil fuel emissions, biospheric fluxes, and atmospheric transport patterns. For example, mid-latitude regions with high anthropogenic emissions may exhibit more immediate responses, while remote or high-latitude regions may show delayed or muted signals.

Several surface in-situ observation sites around the world monitor CO_2 concentrations in the atmosphere, however, surface measurements are more sensitive to local emissions, especially when observation sites are located near high-emission regions, and they are greatly affected by boundary layer dynamics. Total column observations, on the other hand, are less sensitive to local emissions and more representative of regional emissions (Keppel-Aleks et al., 2011). Given their larger spatial footprints, total column measurements provide more information for inverse modeling of regional emissions and trends. Moreover, with

advancements in remote sensing techniques from space, column-averaged dry–air mole fraction of CO_2 can now be measured in remote regions, enabling broader spatial coverage.

The Total Carbon Column Observing Network (TCCON) with 28 stations across four continents, provides long-term ground-based remote sensing observations of CO_2 that are also widely used for validating satellite measurements (Wunch et al., 2010).
55 Satellite missions, such as GOSAT and OCO-2, have been measuring total column CO_2 from space since 2009 and 2014, respectively (Yokota et al., 2009; Crisp, 2015), significantly enhancing global monitoring of CO_2 levels in the atmosphere. These satellite datasets have also been incorporated into the Copernicus Atmosphere Monitoring Service (CAMS), which assimilates measurement data to produce CO_2 flux estimates and gapless total column mole fractions all over the world (Agustí-Panareda et al., 2023).

60 In-situ networks, TCCON, satellite observations, and CAMS reanalysis all offer valuable datasets for investigating CO_2 growth rates across different regions of the world. Several studies have employed ground-based and space-based total column data to examine CO_2 trends and their driving factors. For instance, Lindqvist et al. (2015) compared CO_2 column mole fractions from the GOSAT satellite with measurements from various TCCON stations, providing insights into the seasonal and interannual variability of atmospheric CO_2. Sussmann and Rettinger (2020) developed a framework for deriving annual
65 growth rates from TCCON column-averaged dry-air mole fractions of carbon dioxide (XCO_2) and estimating uncertainties. They applied this method to assess the detectability of COVID-19-related CO_2 emission reductions, highlighting the challenge of distinguishing small anthropogenic signals from natural variability. Buchwitz et al. (2018) used an ensemble-based satellite product to calculate annual CO_2 growth rates both globally and by latitude bands, later refined with updated measurements and an improved ensemble version (Reuter et al., 2020). Extending this work, Labzovskii et al. (2021) analyzed CO_2 growth rates
70 derived from 24 TCCON stations and compared them to results from CarbonTracker, CAMS reanalysis, and satellite-based estimates by Reuter et al. (2020). Collectively, these studies demonstrate how integrating TCCON and satellite data products enhances our understanding of interannual variability in CO_2 growth rates across different regions.

Given the unique opportunity presented by the 2020 emission reductions, we extend the analysis of TCCON-based CO_2 growth rates initially conducted by Sussmann and Rettinger (2020) by incorporating the 2020 measurements, which were
75 not available at the time of their study. To calculate annual growth rates, we examine three previously established methods and identify the most robust approach for our purposes. Our analysis is expanded to include a larger set of TCCON stations, with a focus on the northern temperate regions (30°–50°N), the Arctic, and the Southern Hemisphere. In addition, we leverage modeled data from CAMS, which offer continuous, gap-free time series, to evaluate the consistency of predicted XCO_2 growth rates with TCCON observations, particularly at sites affected by substantial data gaps.
80 Section 2 offers an overview of the measurement sites and modeled products utilized in this study. In section 3, we provide a brief introduction to three methods for calculating annual growth rates and describe their application to our datasets. Section 4 presents the results of the growth rate calculation method analysis, along with the calculated growth rates for each study region based on the most effective method. Finally, section 5 discusses the implications of our findings and explores potential future applications of this analysis.

2 Data

In this analysis, we use XCO_2 measurements from 12 TCCON sites and surface CO_2 in-situ observations from Mauna Loa Observatory (MLO) to compare CO_2 growth rate trends. Although the focus of this study is on total column measurements, MLO is included due to its long-term record, its central role in global CO_2 growth rate assessments (e.g., NOAA GML, UK Met Office analyses (Betts et al., 2024)). In addition its high-altitude location, makes it more representative of the free troposphere and therefore more comparable to total column observations. Additionally, a gridded modeled total column CO_2 product is included for comparison against the observational data.

2.1 In-Situ Measurement Site

The Mauna Loa Observatory provides the longest continuous atmospheric CO_2 record, initiated by the Scripps Institution of Oceanography in 1958 and complemented by NOAA's Global Monitoring Laboratory, which has conducted continuous in-situ measurements since 1974 (Lan et al., 2025; Thoning et al., 2024). For this study, we specifically use the continuous in-situ dataset from NOAA/GML at MLO, which is widely employed for calculating annual growth rates. For example, the UK Met Office uses Mauna Loa data to forecast annual CO_2 growth rates within their seasonal-to-decadal climate models (Betts et al., 2024).

2.2 TCCON Sites

We utilize the XCO_2 data from 12 TCCON sites, the column-averaged dry-air mole fraction of CO_2 retrieved using the GGG software by profile scaling (TCCON Team, 2020; Laughner et al., 2024). The a priori profiles are constructed using meteorological data from the Goddard Earth Observing System Forward Processing for Instrument Teams (GEOS-FP-IT) atmospheric data assimilation system (Lucchesi, 2013). TCCON column retrievals are scaled to the WMO trace gas scale using aircraft- or balloon-based measurements (Laughner et al., 2024).

To investigate the atmospheric response to changes in anthropogenic CO_2 emissions, we choose a subset of TCCON stations in various regions. Recognizing that the majority of fossil fuel emissions occur in the mid-latitudes of the Northern Hemisphere (30-50 °N) and considering the latitudinal gradient in CO_2 we choose three stations in each of the two different latitude bands 40-50 °N and 30-40 °N. We also choose three stations in the high Northern latitudes to investigate the growth rate in the Arctic region. In addition, we consider three stations in the Southern Hemisphere where CO_2 growth is largely influenced by transport from the Northern Hemisphere. From each region, we select sites that have at least five years of data, and have data available up to 2020 and are not located in highly urbanized regions.

We choose three sites from higher latitudes in the Northern Hemisphere: 1. Sodankylä, a rural area located in Northern Finland (Kivi et al., 2022; Kivi and Heikkinen, 2016) ; 2. Ny-Ålesund, which hosts AWIPEV Arctic Research Base on the Svalbard Norwegian island in northern Europe (Buschmann et al., 2022); and 3. Eureka located in Nunavut, which hosts the Polar Environment Atmospheric Research Laboratory (PEARL) (Strong et al., 2022).
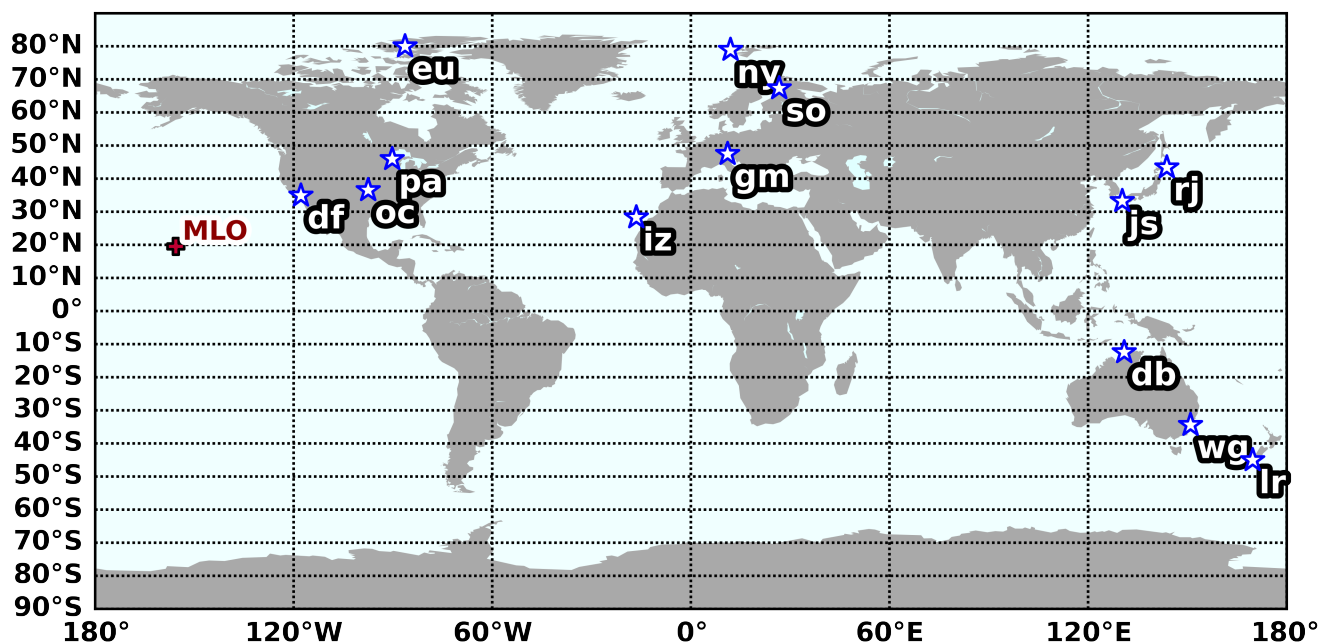
Figure 1. Selected TCCON stations used in this study (marked by white stars). High–latitude NH sites: eu (Eureka), ny (Ny-Ålesund), so (Sodankylä). 40-50 °N latitude band: gm (Garmisch), pa (Park Falls), rj (Rikubetsu), 30-40 °N Latitude band: oc (Lamont), df (Dryden) , js (Saga). Southern Hemisphere sites db (Darwin), wg (Wolangong), lr (Lauder) as well as Izaña (iz) are marked by white stars. The in situ measurement site, Mauna Loa Observatory (MLO), is indicated by a red cross. Global map based on Natural Earth public domain data and plotted using the Cartopy Python library (Met Office, 2024; Natural Earth., 2025).

For the Northern latitude bands 40-–50 degrees North, we choose 1. Park Falls located in Wisconsin USA, within the boreal forest (Wennberg et al., 2022a), 2. Garmisch , located in a small town in Southern Germany in the foothills of the Alps (Sussmann and Rettinger, 2025) ; and 3. Rikubetsu in the island of Hokkaido, Northern Japan, positioned in a rural, mountainous region (Morino et al., 2022).

120   For the Northern latitude bands 30–40 °N, we choose 1. Dryden , California, USA, at the Armstrong Flight Research Center (AFRC) on Edwards Air Force Base (Iraci et al., 2022), desert area, located 150 km northeast of Los Angeles. 2. Lamont , a rural area located in Southern great plains in Oklahoma, USA (Wennberg et al., 2022b). 3. Saga , a small town located in the island of Kyushu in Southern Japan (Shiomi et al., 2022).

    The three Southern Hemisphere stations that meet our time series criteria are: 1. Darwin, Australia, located in Northern
125 Australia (Deutscher et al., 2023b); 2. Wollongong, located in Southeast Australia (Deutscher et al., 2023a); and 3. Lauder, located on New Zealand's South Island (Pollard et al., 2022). Although these stations fall within different latitude bands, the relatively subdued variability in CO_2 levels across the Southern Hemisphere enables meaningful comparisons of CO_2 growth trends by combining data from these locations (Stephens et al., 2013). Data from Darwin and Wollongong are available starting

Table 1. TCCON, in-situ, and CAMS data used for CO_2 growth rate calculation: site locations, measurement periods and average number of measurements per year.

Region	Site Name	Latitude (°)	Longitude (°)	Alt (masl)	Measurement Period	Avg Measurements/yr	Reference
High-Latitude Northern Hemisphere (> 60°N Arctic)	Eureka (eu)	80.05	-86.42	610	2010–2020	3015	Strong et al. (2022)
	Ny-Ålesund (ny)	78.92	11.92	20	2005–2022	6896	Buschmann et al. (2022)
	Sodankylä (so)	67.37	26.63	188	2009–2023	12040	Kivi et al. (2022)
Mid-Latitude Northern Hemisphere (40–50°N)	Garmisch (gm)	47.48	11.06	745	2007–2023	7309	Sussmann and Rettinger (2025)
	Park Falls (pa)	45.94	-90.27	476	2004–2023	21450	Wennberg et al. (2022a)
	Rikubetsu (rj)	43.46	143.77	380	2014–2021	3853	Morino et al. (2022)
Mid-Latitude Northern Hemisphere (30–40°N)	Lamont (oc)	36.60	-97.49	320	2011–2024	29985	Wennberg et al. (2022b)
	Dryden (df)	34.96	-117.88	700	2013–2023	43626	Iraci et al. (2022)
	Saga (js)	33.24	130.29	9	2011–2022	9643	Shiomi et al. (2022)
Southern Hemisphere (SH) (10–50°S)	Darwin (db)	-12.42	130.89	30	2013–2022	21107	Deutscher et al. (2023b)
	Wollangong (wg)	-34.41	150.88	30	2013–2022	7406	Deutscher et al. (2023a)
	Lauder (lr)	-45.04	169.68	370	2004–2023	15432	Pollard et al. (2022)
In-Situ Site	Mauna Loa (MLO)	19.54	155.58	3397	1974–2024	3400	Thoning et al. (2024)
CAMS coverage	Global (1° ×1°)	-90 – 90	-180 – 180	–	2014–2023	2900	Chevallier et al. (2023)

in 2013, while Lauder provides an earlier record beginning in 2010. The 2010–2012 Lauder record used here was provided

130 privately and is not included in the publicly available TCCON files. Accordingly, Lauder is used exclusively to estimate growth rates for 2011–2013, and from 2014 onward, all three sites are included in the Southern Hemisphere average.

Table 1 summarizes the measurement sites used in this study, including their geographic locations, measurement periods, and the average number of individual measurements per year as an indicator of data availability. TCCON measurements are based on roughly 2-minute acquisition intervals and are only taken when sunlight is available, whereas Mauna Loa data consist

135 of hourly averages collected continuously, independent of weather or time of day. Consequently, the number of data points from Mauna Loa is substantially lower. The geographic distribution of the selected sites is shown in Figure 1.

2.3 Modelled Reanalysis Product

CO_2 growth rates derived from TCCON measurements may be subject to biases when significant gaps occur within specific years. Standard TCCON retrievals require direct sunlight and cannot be performed during cloudy conditions or at night, which

140 leads to gaps in the time series. In high-latitude regions, extended periods of low solar elevation or polar night can result in full seasonal gaps, further increasing the risk of seasonal biases in the annual growth rate estimates. On the other hand, reanalysis datasets like those from Carbon Tracker and CAMS (Jacobson et al., 2023; Agustí-Panareda et al., 2023; Chevallier, 2024) address these gaps by using model estimations. This approach enables the examination of how gaps in measurement data could affect annual growth rate calculations. In this study, we use the CAMS Reanalysis XCO_2 total column product, which

145 assimilates satellite retrievals from OCO-2 together with surface and aircraft observations to provide a comprehensive estimate of atmospheric CO_2. The data have a spatial resolution of $1.4° \times 0.7°$ and a 3-hourly temporal resolution, spanning from 2014 to 2023 (Chevallier, 2024).

3 Methods

Accurately calculating annual CO_2 growth rates is critical for understanding atmospheric trends and identifying regional dif-
ferences. In this study, we evaluate three commonly used methods to assess their robustness and sensitivity to data gaps,
particularly at sites with limited observational coverage. A sensitivity analysis is performed to examine how data availability
affects growth rate estimates by applying these methods to both TCCON measurements and CAMS satellite reanalysis data at
sites with the most pronounced data gaps. Finally, we apply the most reliable method, based on this evaluation, to the regionally
averaged time series for each study region.

3.1 Data Preparation

For TCCON, we use the publicly available dataset processed with GGG2020 (TCCON Team, 2020; Laughner et al., 2024),
excluding CO_2 measurements with errors exceeding 3 ppm to ensure high data quality. MLO in-situ measurements are filtered
using the dataset's quality control flags. These datasets differ in temporal resolution: TCCON provides measurements every 2
minutes whenever sufficient solar radiation is available, MLO data are reported hourly, and CAMS reanalysis offers continuous,
gap-free data at 3-hour intervals.

To account for atmospheric variability on synoptic scales, we compute weekly averages following the approach of Sussmann
and Rettinger (2020). To ensure consistency, we analyze TCCON and MLO data starting from 2010 and align comparisons
with CAMS reanalysis data from 2014 onward. For spatial consistency, we use the CAMS grid point nearest to each TCCON
site.

Regional growth rates are calculated by averaging the weekly time series from stations within each region, which reduces the
influence of outliers and increases sampling density. This results in narrower confidence intervals and a more representative,
stable regional trend. Although data availability varies across sites—sometimes causing unequal contributions—combining
multiple stations overall improves estimate robustness.

3.2 Growth Rate Calculation Methods

We examine three previously established methods to estimate annual CO_2 growth rates: the Monthly Mean (MM), Fourier
Fit residuals (FF), and Dynamic Linear Model (DLM). The growth rate here refers to the increase in atmospheric CO_2 con-
centration, expressed in parts per million per year (ppm/yr), calculated over a one-year period. Each method is applied to
weekly averaged data to minimize short-term variability and to maintain consistency across datasets with differing temporal
resolutions. These three methods were selected based on their prior use in similar studies and their suitability for datasets with
varying temporal coverage and data density.

3.2.1 Monthly Mean (MM)

The Monthly Mean (MM) method, originally introduced by Buchwitz et al. (2018) for satellite observations and later applied to
TCCON ground-based measurements by Labzovskii et al. (2021), estimates annual growth rates by first computing the average

CO$_2$ value for each calendar month m (e.g., January, February, etc.) in each year y, denoted as $C_{y,m}$. This yields up to 12
180 monthly averages per year. Monthly growth rates are then calculated by differencing the same months from consecutive years,
i.e., $\Delta C_{y,m} = C_{y,m} - C_{y-1,m}$. The annual growth rate for year y is then obtained by averaging the available monthly growth
rates as

$$\mathrm{gr}_y = \frac{1}{N_y} \sum_{m=1}^{N_y} \Delta C_{y,m} \qquad (1)$$

where N_y is the number of months with valid data in both year y and year $y-1$. The associated uncertainty is estimated
185 by calculating the standard deviation σ_y of the $\Delta C_{y,m}$ values and scaling it to account for incomplete month coverage, i.e.,
$\delta\mathrm{gr}_y = \sigma_y \cdot \sqrt{12/N_y}$. This method is valued for its simplicity and ease of implementation; however, it is sensitive to data gaps,
as missing months may reduce N_y and potentially introduce biases in the estimated annual growth rates.

3.2.2 Fourier Fit (FF)

The Fourier Fit (FF) method combines linear regression with a Fourier series to model the long-term trend and seasonal cycle
190 in CO$_2$ time series, as described by Sussmann and Rettinger (2020). The fit is expressed as $F(t, a_0, a_1, b_1, \ldots, b_8)$, where a_0
is the intercept, a_1 is the slope of the linear trend, and b_1 to b_8 are the Fourier coefficients for four annual harmonics. The
residuals are calculated as the difference between the measured CO$_2$ values M and the model fit: $M - F(t)$. These residuals
represent deviations from the overall trend at each time step and are used to quantify annual offsets.

For each year, a constant offset $a_{0,\mathrm{yr}}$ is fitted to the residuals, representing how that year's median deviates from the overall
195 fit. The annual growth rate is then calculated as the difference in these offsets between consecutive years, added to the linear
trend term a_1, as follows:

$$\mathrm{gr}_{\mathrm{yr}} = a_{0,\mathrm{yr}} - a_{0,\mathrm{yr}-1} + a_1 \qquad (2)$$

This formulation captures both the long-term linear increase in CO$_2$ and interannual deviations from the trend. Confidence
intervals are estimated using bootstrap resampling with 5,000 iterations, following Sussmann and Rettinger (2020), with the
200 2.5th and 97.5th percentiles defining the 95% confidence interval.

3.2.3 Dynamic Linear Model (DLM)

The Dynamic Linear Model (DLM) is a statistical framework well suited for analyzing time series with irregular sampling
and data gaps. It was, for example, applied by Laine (2020) to analyze ozone trends in the atmosphere, and later adapted for
satellite-based methane retrievals by Hachmeister et al. (2024). For this analysis, we use the `dlmhelper` package developed
205 by Hachmeister (2025), which streamlines the application of DLMs in atmospheric datasets.

We determine the best-fit model from an ensemble of DLMs with different numbers of harmonic components (1, 2, 3, or 4), selecting the configuration that yields the lowest total covariance level. In most regions, the best performance is obtained using four harmonics, while in the Arctic region, only one harmonic is selected.

We apply the DLM to fit weekly time series of XCO_2, providing estimates of the underlying CO_2 levels at that temporal resolution. The DLM method provides a fit on the same time resolution as the input data, so using weekly input results in a weekly-resolved growth rate time series. From this, we calculate annual growth rates as the difference between deseasonalized annual means of the DLM fit in consecutive years:

$$\text{gr}_{\text{yr}}^{\text{DLM}} = \mu_{\text{yr}} - \mu_{\text{yr}-1} \tag{3}$$

where μ_{yr} is the mean of the deseasonalized, detrended DLM fit for year yr. The associated uncertainty in each annual growth rate is estimated as the square root of the sum of the annual level covariances from adjacent years, i.e., $\sigma_{\text{gr,yr}}^{\text{DLM}} = \sqrt{\sigma_{\mu,\text{yr}}^2 + \sigma_{\mu,\text{yr}-1}^2}$. Uncertainties tend to be larger at the beginning and end of the time series due to edge effects.

3.2.4 Method Evaluation and Selection

To assess the robustness of the three methods, we evaluate them at three sites with varying data coverage. Mauna Loa (MLO) offers high-quality, near-continuous hourly in-situ measurements, including nighttime observations. Lamont, a TCCON site located in a region with frequent sunlight, provides a dense and consistent dataset. In contrast, Eureka, a high-latitude TCCON site, experiences sparse measurements a pronounced data gap during the polar night in winter due to the absence of sunlight.

To evaluate the impact of such data gaps in a high-latitude context, we conduct a sensitivity analysis at Eureka using the gap-free CAMS reanalysis dataset. Growth rates are first calculated using the complete CAMS time series, then recalculated after downsampling the dataset to match the temporal coverage of the TCCON measurements. This comparison reveals the method most resilient to missing data, which is subsequently applied to the regionally averaged TCCON time series across the four study regions.

4 Results

4.1 Growth rate calculation method comparison

To evaluate the performance of different growth rate calculation methods, we applied three approaches to the three representative sites selected in Section 2.2. We used all available data from 2009 onward, allowing annual growth rates to be derived starting in 2010. Figure A1 displays the time series of measurements from the three stations. The MLO in-situ measurements cover the entire period, except for a gap from December 2022 to July 4, 2023, caused by the Mauna Loa Volcano eruption (Thoning et al., 2024). Lamont TCCON measurements began in April 2011, allowing for annual growth rate calculations from 2012 onward. Eureka has data available from 2010, but there are no measurements for 2012 and 2013. Furthermore, measure-

235   ments were interrupted in July 2020 due to instrument issues that could not be addressed due to COVID-19 travel restrictions, limiting growth rate calculations to data available through 2020.

Figure 2 presents annual growth rate estimates and the associated uncertainty ranges at each station using the three different methods. While each method uses its own approach to estimate uncertainties, a qualitative comparison shows that the Monthly Mean method tends to produce broader uncertainty ranges, making it more difficult to resolve year-to-year changes. By con-

240   trast, the Fourier Fit and DLM methods yield comparatively smaller uncertainty ranges, as evaluated within each method's framework.

At Eureka, the DLM interpolates growth rates during the 2012–2014 gap. However, these estimates must be interpreted with caution, as they rely on the assumption of smooth variation, and cannot capture potential short-term fluctuations similar to those seen at Lamont and MLO during that period.

245   At MLO and Lamont, the growth rates from all three methods show close agreement. At Eureka, a notable discrepancy appears in 2019 between the DLM estimate and the other two methods, possibly due to data sparsity at this station. The following section explores the sensitivity of each method to data gaps in more detail.

4.1.1   Gap sensitivity analysis

Figure A2 presents the CAMS reanalysis XCO_2 time series overlaid with TCCON measurements at Eureka. This overlay

250   demonstrates the practical advantage of using CAMS in Arctic regions, where TCCON observations are frequently unavailable due to polar night or instrument downtime. To assess whether the observed differences in growth rate estimates between TC-CON and CAMS stem from actual variability or are primarily driven by data availability, the CAMS dataset was downsampled to match the temporal coverage of the TCCON measurements.

To perform the downsampling, the high-frequency TCCON data were first averaged into 3-hourly means to match the

255   native temporal resolution of the CAMS reanalysis. Next, both time series were merged by timestamp, and only 3-hourly intervals where both TCCON and CAMS had valid data were retained. This allowed the CAMS dataset to be filtered such that its temporal coverage mirrored that of TCCON. The resulting downsampled CAMS data were then averaged into weekly means—consistent with the treatment of other datasets—prior to applying the growth rate calculation methods. The downsampled CAMS time series is also included in Figure A2 for reference. The analysis period was restricted to 2014 onward to match

260   the start date of the CAMS reanalysis product.

For both the TCCON and downsampled CAMS datasets, the DLM ensemble member with the lowest level covariance corresponded to a configuration with only one seasonal parameter, which we selected for our analysis. Similarly, for the FF method, we initially applied four harmonics as used for other stations, but significant data gaps in the Eureka record led to overfitting. To improve the stability of the fit and align with the DLM configuration, we reduced the model to a single seasonal

265   parameter. The MM method does not involve curve fitting and instead relies on the available monthly data. Due to the relatively sparse measurements at Eureka, the MM approach resulted in broader uncertainty ranges reflecting the smaller sample size.

Figure 3 illustrates the annual CO_2 growth rates at Eureka, derived from both TCCON measurements and CAMS reanalysis data. For the TCCON dataset (solid bars), all three methods produce broadly consistent growth rates, except for 2019, as noted
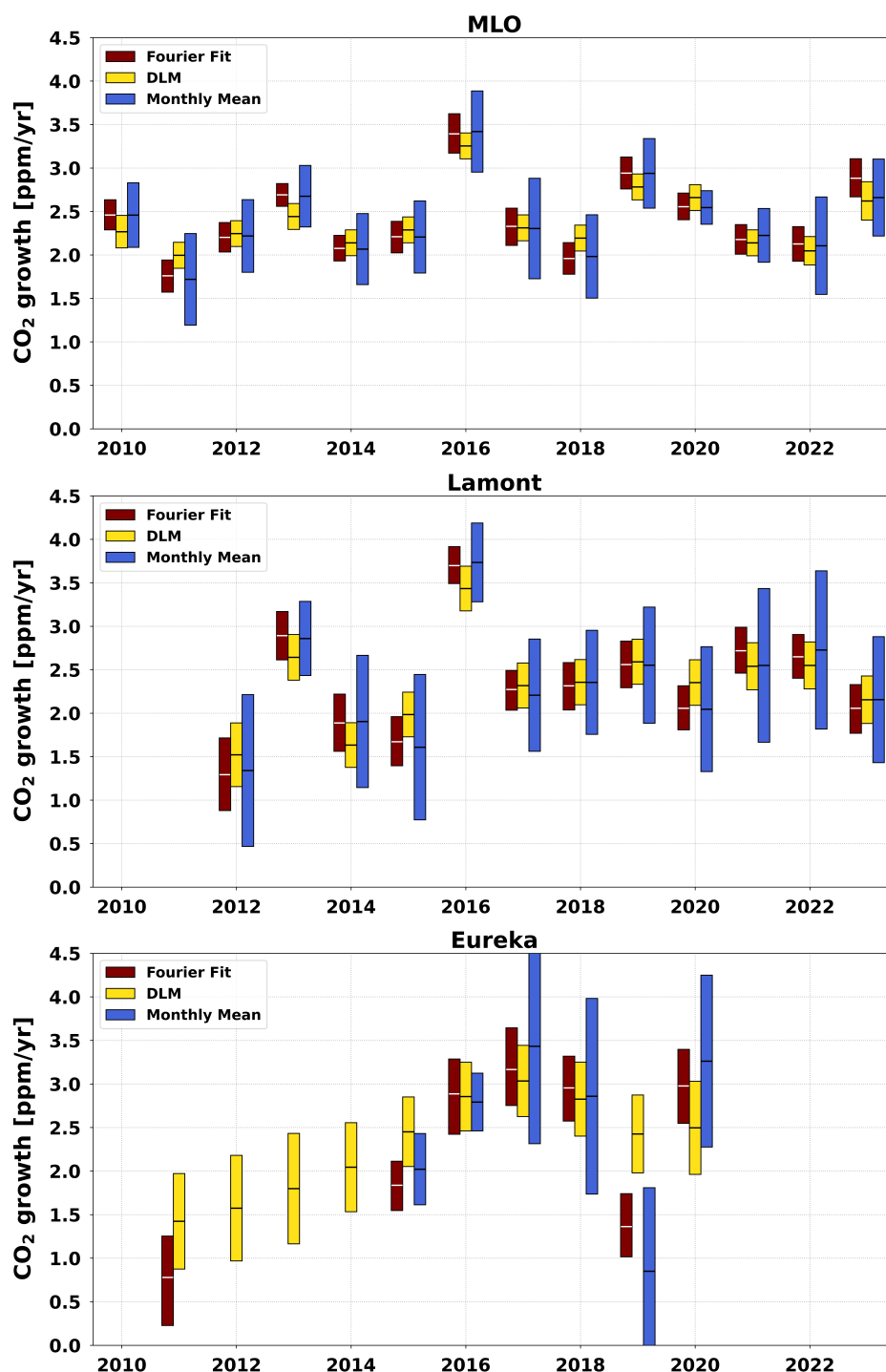
Figure 2. Annual CO_2 growth rates are plotted by year for each of the three sample sites using three different methods. The central line within each bar indicates the median growth rate, and the bar length reflects the associated uncertainty, which is defined separately for each method.

earlier. The MM method (blue) shows larger uncertainties, in line with its statistical formulation, making it less sensitive to
270 interannual variability. In contrast, the DLM (yellow) and FF (maroon) methods exhibit sharper year-to-year changes.

When applied to full-resolution CAMS data, all three methods agree well within uncertainty across all years (hatched bars).
For the downsampled CAMS dataset (dotted bars), which mimics TCCON's temporal availability, the absence of data in 2014
prevents growth rate calculation for 2015. In subsequent years, the FF and MM methods exhibit noticeable shifts in mean
growth rates compared to full-resolution CAMS, particularly in 2016–2017—suggesting these methods are more sensitive to
275 sampling density. The DLM method appears least affected by downsampling, with results (hatched yellow) staying within the
envelope of both the full CAMS and TCCON estimates, including in 2019.

In 2019, which was previously identified as a year with atypical behavior in the TCCON dataset, the DLM method remained
notably stable across all datasets, indicating greater robustness to data irregularities or gaps. In contrast, the FF and MM
methods exhibited shifts that aligned more closely with the original TCCON growth rates. While FF yields similar results in
280 most cases, DLM's stability under irregular sampling makes it a more reliable choice. The MM method, while useful for cross-
checking, lacks the resolution needed to detect interannual signals of interest. For this reason, we choose the DLM method for
investigating growth rates in different regions of the world.
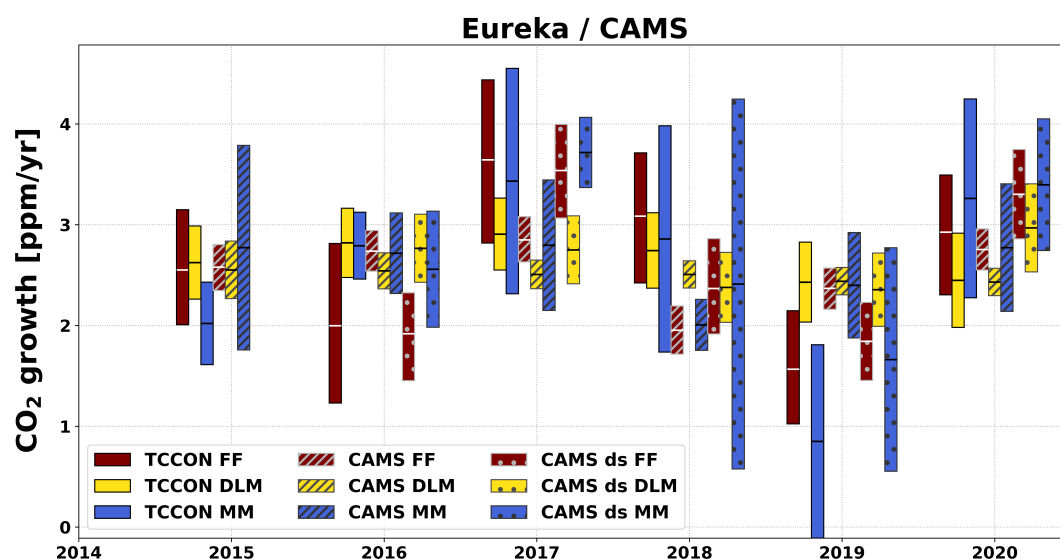
Figure 3. Annual CO_2 growth rates plotted for Eureka and the closest CAMS grid point original and downsampled (ds) to match the TCCON
measurements, using the three approaches for calculating growth rate. The x-axis represents calendar years. The central line within each bar
indicates the median growth rate, and the bar length reflects the associated uncertainty, which is defined separately for each method.

4.2 Interannual variations in CO$_2$ growth rates

Figure 4 illustrates the interannual variations in CO$_2$ growth rates across the four TCCON study regions and the MLO in situ
285 site, overlaid with fossil fuel emissions from the Emissions Database for Global Atmospheric Research (EDGAR) database
(Crippa et al., 2023). Detailed annual growth rates for individual sites within each region are provided in Figure A4.

Overall, CO$_2$ growth rate trends show broad agreement across regions, despite year-to-year variability. Long-term average
growth rates are remarkably similar—around 2.4 ppm/year—for the Arctic, 30–40°N, 40–50°N, and MLO in situ, with un-
certainties ranging from ± 0.3 to ± 0.5 ppm/year. The Southern Hemisphere shows a growth rate of 2.3 ± 0.6 ppm/year. The
290 reported uncertainties represent the standard deviation of annual growth rates, reflecting interannual variability. The overlap-
ping uncertainty ranges indicate consistent long-term CO$_2$ growth trends across these spatial domains.

To better illustrate the interannual variability, Table 4.2 presents the CO$_2$ growth rate anomalies alongside ENSO conditions
and fossil fuel emission changes. In 2016, a year marked by a strong El Niño event, all regions exhibited statistically significant
increases in CO$_2$ growth rates compared to 2015, with most sites showing large absolute increases exceeding 1 ppm/year. An
295 exception is the 40–50°N region, which showed a smaller but still statistically significant increase of +0.7 ppm/year.

In 2020, following a notable 5% reduction in fossil fuel CO$_2$ emissions, a distinct divergence in growth rates is observed
across regions. While the MLO site shows only a slight decline compared to 2019, the Arctic and Southern Hemisphere
exhibit modest increases, but these changes fall within the range of interannual variability and are not statistically significant.
In contrast, the 40–50°N region shows a statistically significant increase in growth rate. Meanwhile, the 30–40°N region
300 experiences a statistically significant decrease compared to 2019; however, the magnitude of this decline (–0.4 ppm/year) is
modest relative to changes observed during strong ENSO years. Given the substantial drop in anthropogenic emissions, the
decrease in this densely urbanized latitude band likely reflects a regional sensitivity to reduced fossil fuel activity—an effect not
clearly observed elsewhere. This interpretation is supported by fossil fuel emissions maps from EDGAR (Figure A5), which
show that the majority of anthropogenic CO$_2$ emissions occur within the 30–40°N latitude band where there's a large portion
305 of urban areas. In 2020, large emission reductions are observed in countries such as Japan and the USA further reinforcing the
link between localized emission changes and observed growth rate anomalies in this region.

The plot also highlights the influence of strong and moderate La Niña events on regional CO$_2$ growth rate patterns. In 2011,
during a strong La Niña, a statistically significant decline in growth rates is observed in the 40–50°N region and the Arctic. This
was followed by a moderate La Niña in 2012, after which all regions experienced increases in growth rates, likely reflecting
310 a rebound from the preceding strong La Niña. In 2013, northern mid-latitudes saw growth rates rise by an additional 0.8–1.2
ppm/year relative to 2012. These increases are possibly the result of the combined effects of the transition out of the two-year
La Niña phase and a concurrent rise in anthropogenic CO$_2$ emissions, which followed a steady upward trajectory between
2010 and 2013.

A similar pattern is observed during the 2021–2022 La Niña period: CO$_2$ growth rates declined at MLO and in the Southern
315 Hemisphere, while the Arctic and northern high latitudes showed little change in 2021. Notably, the 30–40°N region exhibited
a statistically significant increase that year, likely reflecting a rebound in fossil fuel emissions after the COVID-19 reductions.

However, by 2022, the continued La Niña conditions appear to have exerted a broader suppressive effect on CO_2 growth rates across multiple regions. This declining trend persisted into 2023 for all TCCON regions, with particularly significant decreases in the 30–40°N and 40–50°N latitude bands, while MLO showed a rebound. These results highlight the spatial heterogeneity of biospheric and atmospheric responses to ENSO variability and suggest the need for further analysis to better understand the underlying mechanisms.

Figure 5 further explores the relationship between ENSO strength and the calculated CO_2 growth rates in each region. Positive ENSO values correspond to El Niño events, while negative values indicate La Niña conditions. We adopt the ENSO strength classification used by Labzovskii et al. (2021), which ranges from –3 for strong La Niña to +4 for very strong El Niño, consistent with the Oceanic Niño Index (ONI) classifications provided by NOAA (https://ggweather.com/enso/oni.htm). To account for the lag between oceanic temperature anomalies and their influence on the carbon cycle, we associate the second year of each two-year ENSO phase with the atmospheric response. This lag reflects the time needed for sea surface temperature changes to affect biospheric activity and CO_2 fluxes.

The correlation analysis reveals no statistically significant relationship between ENSO strength and CO_2 growth rates in the Arctic, 40–50°N, or 30–40°N regions (P-values > 0.05). In contrast, significant correlations with low P-values and high R^2 values are found for the Southern Hemisphere and MLO, suggesting a stronger sensitivity to ENSO-driven variability in these regions.
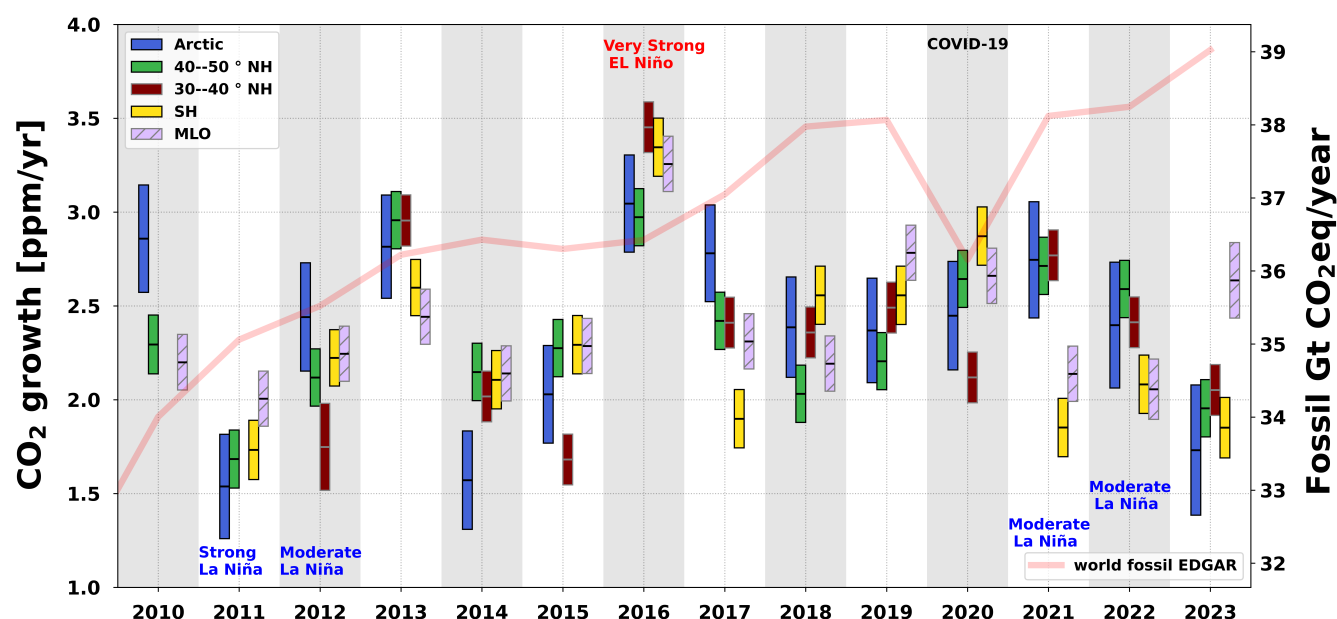
Figure 4. Annual growth rates and their uncertainty ranges for the four TCCON regions and MLO, calculated using the DLM method shown by year. The central line within each bar indicates the median growth rate, and the bar length reflects the associated uncertainty. The red line represents global fossil fuel CO_2 emission trends from EDGAR.

Table 2. Annual CO_2 growth rate anomalies (in ppm/year and percentage change relative to the previous year in parentheses) for various regions and the Mauna Loa Observatory (MLO), shown alongside fossil fuel emission changes (from EDGAR) and ENSO classifications. Statistical significance is based on the overlap of uncertainty ranges: anomalies are considered significant when there is no overlap, and moderately significant when the change exceeds half the combined uncertainty. Color shading highlights positive (red) and negative (blue) anomalies using dark shading for strong significance, medium shading for moderate significance, and light shading for marginal significance.

Year	Arctic	40–50°N	30–40°N	SH	MLO	Fossil Emissions	ENSO Condition
2011	−1.3 (-46%)	−0.6 (-27%)	–	–	−0.2 (-9%)	+3.1%	strong La Niña
2012	+0.9 (+60%)	+0.5 (+29%)	–	+0.7 (+51%)	+0.2 (+12%)	+1.3%	moderate La Niña
2013	+0.4 (+16%)	+0.9 (+40%)	+1.2 (+68%)	+1.2 (+54%)	+0.2 (+9%)	+2.0%	neutral
2014	−1.3 (-45%)	−0.9 (-29%)	−0.9 (-32%)	−1.3 (-39%)	−0.3 (-12%)	+0.6%	neutral
2015	+0.5 (+31%)	+0.2 (+8%)	−0.3 (-16%)	+0.2 (+10%)	+0.1 (+7%)	−0.4%	weak El Niño
2016	+1.0 (+49%)	+0.7 (+30%)	+1.7 (+103%)	+1.1 (+48%)	+1.0 (+42%)	+0.3%	very strong El Niño
2017	−0.3 (-9%)	−0.5 (-19%)	−1.0 (-30%)	−1.5 (-43%)	−0.9 (-29%)	+1.7%	weak La Niña
2018	−0.4 (-14%)	−0.4 (-16%)	−0.0 (-2%)	+0.6 (+33%)	−0.1 (-5%)	+2.5%	weak La Niña
2019	−0.0 (-1%)	+0.2 (+8%)	+0.1 (+5%)	+0.0 (+1%)	+0.6 (+27%)	+0.2	weak El Niño
2020	+0.1 (+4%)	+0.4 (+20%)	−0.4 (-15%)	+0.3 (+12%)	−0.1 (-4%)	−5.0%	neutral
2021	+0.3 (+12%)	+0.1 (+2%)	+0.7 (+32%)	−1.0 (-35%)	−0.5 (-20%)	+5.4%	moderate La Niña
2022	−0.5 (-17%)	−0.1 (-5%)	−0.4 (-14%)	+0.3 (+14%)	−0.1 (-4%)	+0.3%	moderate La Niña
2023	−0.4 (-18%)	−0.6 (-24%)	−0.3 (-14%)	−0.3 (-16%)	+0.6 (+28%)	+2.0%	weak La Niña

5 Conclusions

TCCON provides a valuable dataset for investigating regional CO_2 growth rates globally. While TCCON measurements offer
precise and consistent data, regional variations in station coverage introduce uncertainties, particularly in areas with sparse
or intermittent observations. Using multiple stations within a region increases data density, helping to reduce uncertainty in
regional growth rate estimates. Particularly in high-latitude regions, winter data gaps can introduce biases when calculating an-
nual CO_2 growth rates, but the Dynamic Linear Model further improves trend estimation by dynamically adapting to changing
growth rates and effectively handling data gaps—an essential capability given the inherently discontinuous nature of TCCON
data. Furthermore, comparison with CAMS reanalysis shows good agreement with TCCON, indicating that even where TC-
CON data are absent, CAMS can provide consistent growth rate estimates.

Noticeable changes in annual growth rates can be observed in years affected by specific ENSO events or anthropogenic
emission shifts. A relatively strong correlation is found between growth rates at Mauna Loa and in the Southern Hemispheric
TCCON sites with ENSO strength, whereas other regions show no clear relationship. This spatial variability likely arises from
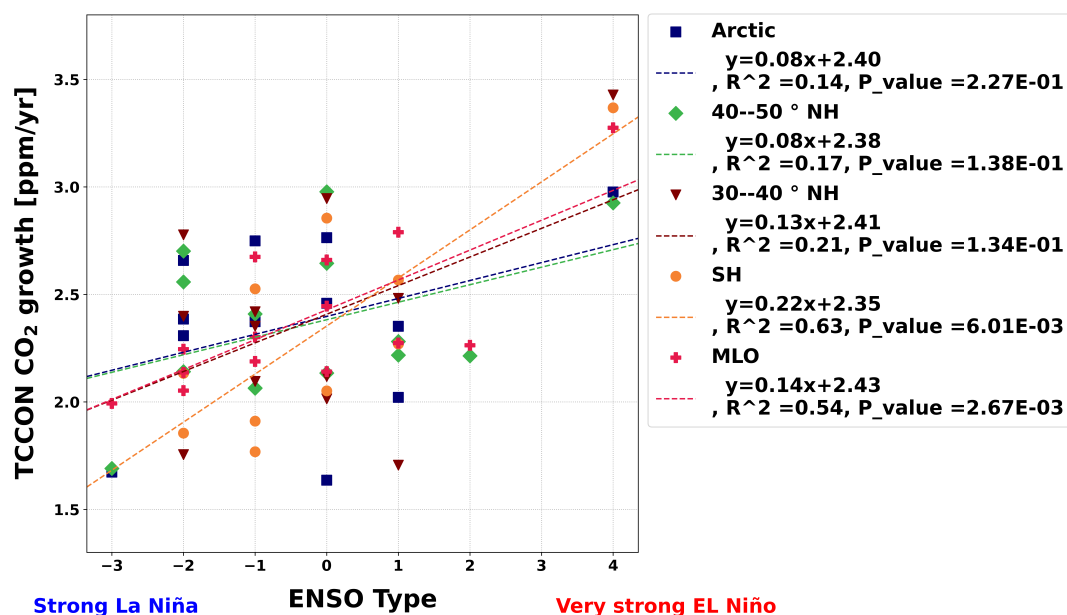
Figure 5. Correlation between TCCON calculated growth rates in four regions and MLO growth rates vs the ENSO strength each year as defined by NOAA.

345   a combination of factors, including differences in biospheric sensitivity to ENSO events. For instance, Zhang et al. (2019) demonstrate that tropical and arid/semiarid regions—such as large parts of Australia—are among the most sensitive to ENSO variability in terms of gross primary production (GPP). The 2020 case study indicates that the 30–40°N latitude band exhibits a stronger sensitivity to changes in fossil fuel emissions, likely due to its higher baseline anthropogenic activity.

     In-situ measurements at the MLO site provide valuable insights into changes in atmospheric CO_2 mole fractions in response
350   to climate variability. However, extending this analysis to include TCCON measurements from different regions enhances our understanding of CO_2 trends in relation to policy-driven emission reductions. Regional growth rate estimates derived from TCCON can serve as independent validation tools for emission inventories and climate policies, particularly in regions with strong fossil fuel sources. This highlights the importance of maintaining and expanding the TCCON network to support long-term atmospheric monitoring and climate mitigation efforts.

355   Although this study focused on regions with long-term TCCON measurements, an important next step is to extend the analysis to under-observed areas that lack TCCON coverage. By leveraging the CAMS reanalysis product's global, gap-free coverage, along with satellite datasets from missions such as OCO-2, OCO-3, and GOSAT, it will be possible to infer CO_2 growth rates in regions such as Africa, South America, and Southeast Asia. This expanded analysis will help assess whether trends observed in well-sampled regions are globally representative and could support the development of robust, region-
360   specific emission verification systems. It may also provide valuable insights for countries that are currently data-sparse but are significant contributors to global emissions.

Code and data availability. The TCCON retrievals are available from the Caltech library at https://tccondata.org/. In-situ observation data from the Mauna Loa Observatory (MLO) are available from https://gml.noaa.gov/data/. CAMS global inversion-optimised CO_2 mean column values are available from https://ads.atmosphere.copernicus.eu/. CO_2 annual and gridded emissions are available from the EDGAR database: https://edgar.jrc.ec.europa.eu/dataset_ghg2024. The DLM code used to fit the CO_2 time series and calculate annual growth rates is available at https://doi.org/10.5281/zenodo.14772372.

Appendix A: Supplementary figures
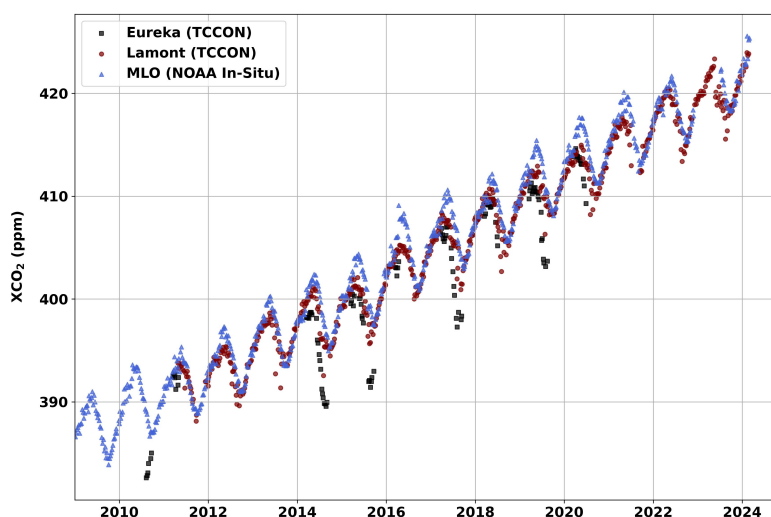
Figure A1. Time series of weekly averaged ground-level CO_2 concentrations from the NOAA MLO site and weekly averaged XCO_2 measurements from the Lamont and Eureka TCCON sites
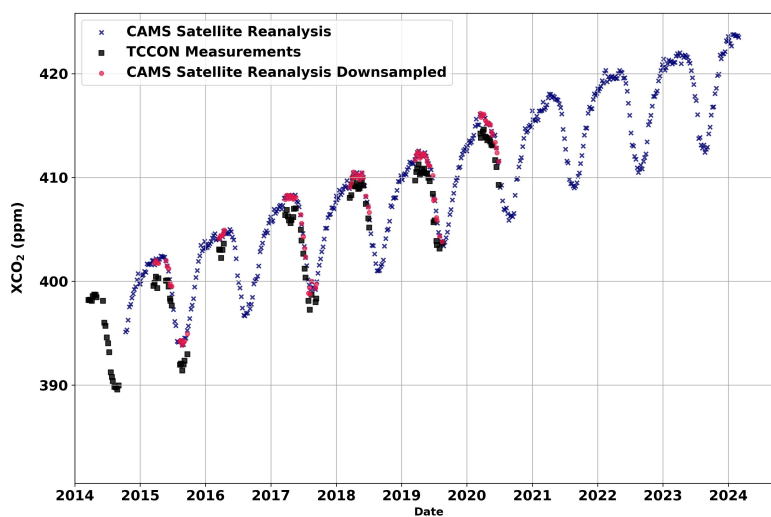
Figure A2. Time series of weekly averaged XCO_2 from the Eureka TCCON overlaid with CAMS reanalysis data from the nearest grid point to each as well as the downsampled CAMS timeseries.
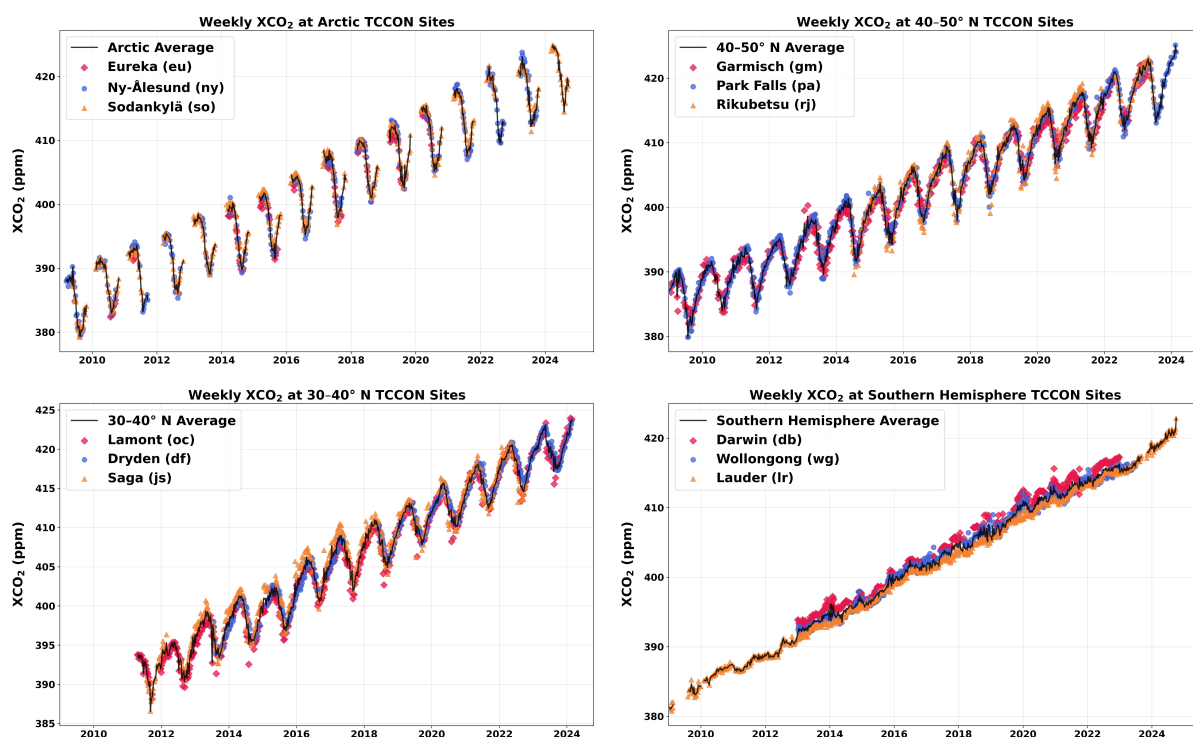
Figure A3. Time series of weekly XCO_2 measurements from selected TCCON stations and regional averages, covering the period from 2009 to 2024. Each panel corresponds to a different study region: (top left) Arctic sites, (top right) 40–50°N, (bottom left) 30–40°N, and (bottom right) Southern Hemisphere sites. Colored markers represent individual TCCON station measurements, while the black line shows the smoothed regional average, with gaps masked where data is not available.
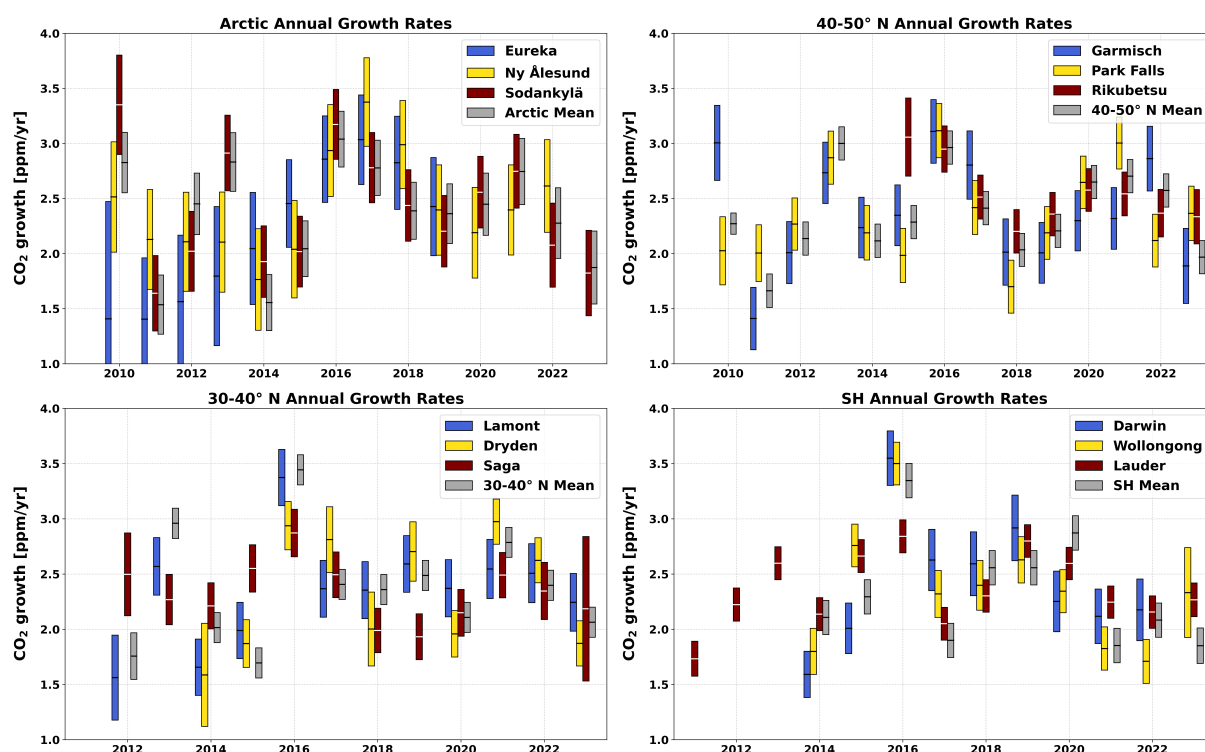
Figure A4. Annual CO$_2$ growth rates derived from TCCON stations, covering 2009–2024. Each panel corresponds to a different study region: (top left) Arctic sites, (top right) 40–50°N, (bottom left) 30–40°N, and (bottom right) Southern Hemisphere sites. Colored bars show annual growth rates for individual stations, and grey bars indicate the average of all sites within the region. The central line within each bar indicates the median growth rate, and the bar length reflects the associated uncertainty.
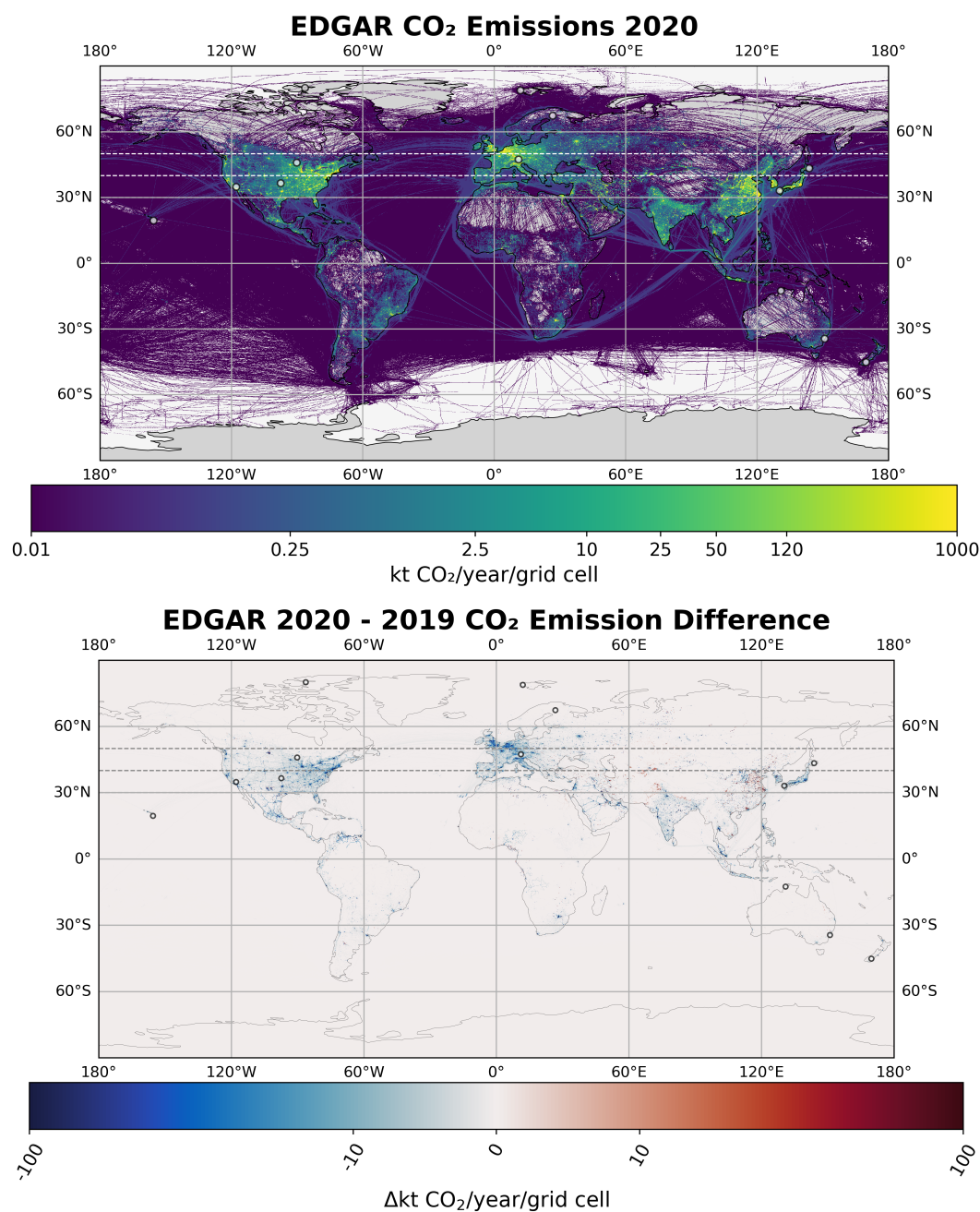
Figure A5. Top: Map of 2020 fossil fuel emissions based on the EDGAR 2020 fossil fuel flux data, displayed at a $0.1°×0.1°$ resolution (Crippa et al., 2023). Bottom: Map showing the difference in emissions between 2020 and 2019 at the same resolution. The locations of TCCON stations used in this study are marked with yellow circles, while additional horizontal lines at 40°N and 50°N are added to indicate the latitude bands used for regional analysis. Global map based on Natural Earth public domain data and plotted using the Cartopy Python library (Met Office, 2024; Natural Earth., 2025).

Author contributions. **Nasrin Mostafavi Pak**: Conceived and designed the study. Performed the growth rate analysis and method compar-
370 isons. Ran the Garmisch TCCON retrievals and prepared all plots and figures. Wrote the manuscript and integrated coauthor feedback. **Jonas
Hachmeister**: Provided the DLM code, made necessary adjustments for this study, and supported the development of the analysis. **Markus
Rettinger**: Provided the code for the FF growth rate calculation and collected the Garmisch raw data. **Matthias Buschmann**: Provided
Ny-Ålesund TCCON data and provided feedback leading to improvements to the manuscript. **Nicholas Deutscher**: Provided Wollongong
TCCON data. **David W. T. Griffith**: Provided Darwin TCCON data. **Laura T. Iraci**: Provided Dryden TCCON data. **Xin Lan**: Provided
MLO GML NOAA data. **Erin McGee**: Processed Eureka TCCON data. **Isamu Morino**: Provided Rikubetsu TCCON data. **Dave Pollard**:
375 Provided Lauder TCCON data. **Coleen M. Roehl**: Processed Dryden and Lamont TCCON data. **Kimberly Strong**: Provided Eureka TC-
CON data. **Rigel Kivi**: Provided Sodankylä TCCON data. **Paul Wennberg**: Provided Dryden and Lamont TCCON data. All authors read
and approved the manuscript.

Competing interests. The authors declare no conflict of interest.

Acknowledgements. This research was supported by the German Federal Ministry of Research, Technology and Space (BMFTR) through
380 its project ACTRIS-D (Aerosols, Clouds and Trace gases Research Infrastructure), which provided personal funding for SM and essential
support and resources for the data collection and analysis presented in this manuscript, and to the Helmholtz Research Program "Changing
Earth", Topic 1 "The Atmosphere in Global Change" at KIT. The authors acknowledge Dr. Ralf Sussmann (KIT/IMK-IFU) for providing the
Garmisch TCCON data and Dr. Kei Shiomi (JAXA) for providing the Saga TCCON data used in this study.

The Eureka TCCON (Strong et al., 2022) measurements were made at the Polar Environment Atmospheric Research Laboratory (PEARL)
385 by the Canadian Network for the Detection of Atmospheric Change (CANDAC), primarily supported by the Natural Sciences and Engineer-
ing Research Council of Canada, Environment and Climate Change Canada, and the Canadian Space Agency. The author gratefully acknowl-
edges NASA, the California Institute of Technology (Caltech), and the Jet Propulsion Laboratory (JPL) for the OCO-2 and OCO-3 missions,
which made this work possible. The TCCON station located at NASA's Armstrong Flight Research Center (formerly Dryden) is supported
by NASA's Earth Science Division. The TCCON site at Rikubetsu is supported in part by the GOSAT series project. Darwin and Wollon-
390 gong TCCON stations are supported by Australian Research Council grants DP160100598, DP140101552, DP110103118, DP0879468, and
LE0668470, and NASA grants NAG512247 and NNG05GD07G. TCCON activities at the Lauder site are supported by the New Zealand
Ministry of Business, Innovation and Employment Strategic Science Investment Fund. The author thanks ChatGPT (GPT-5, OpenAI) for
valuable assistance in code debugging and improving the clarity of the manuscript.

References

395   Agustí-Panareda, A., Barré, J., Massart, S., Inness, A., Aben, I., Ades, M., Baier, B. C., Balsamo, G., Borsdorff, T., Bousserez, N., Boussetta, S., Buchwitz, M., Cantarello, L., Crevoisier, C., Engelen, R., Eskes, H., Flemming, J., Garrigues, S., Hasekamp, O., Huijnen, V., Jones, L., Kipling, Z., Langerock, B., Mcnorton, J., Meilhac, N., Noël, S., Parrington, M., Peuch, V. H., Ramonet, M., Razinger, M., Reuter, M., Ribas, R., Suttie, M., Sweeney, C., Tarniewicz, J., and Wu, L.: Technical note: The CAMS greenhouse gas reanalysis from 2003 to 2020, Atmos. Chem. Phys, 23, 3829–3859, https://doi.org/10.5194/acp-23-3829-2023, 2023.

400   Betts, R. A., Jones, C. D., Knight, J. R., Pope, J. O., and Sandford, C.: Mauna Loa carbon dioxide forecast for 2024 -, Tech. rep., Met Office, https://www.metoffice.gov.uk/research/climate/seasonal-to-decadal/long-range/forecasts/co2-forecast, 2024.

Buchwitz, M., Reuter, M., Schneising, O., Noël, S., Gier, B., Bovensmann, H., Burrows, J. P., Boesch, H., Anand, J., Parker, R. J., Somkuti, P., Detmers, R. G., Hasekamp, O. P., Aben, I., Butz, A., Kuze, A., Suto, H., Yoshida, Y., Crisp, D., and O'Dell, C.: Computation and analysis of atmospheric carbon dioxide annual mean growth rates from satellite observations during 2003-2016, Atmos. Chem. Phys, 18,

405   17 355–17 370, https://doi.org/10.5194/ACP-18-17355-2018, 2018.

Buschmann, M., Petri, C., Palm, M., Warneke, T., and Notholt, J.: TCCON data from Ny-Alesund, Svalbard (NO), Release GGG2020.R0, https://doi.org/10.14291/TCCON.GGG2020.NYALESUND01.R0, 2022.

Chevallier, F.: Description of the CO_2 inversion production chain - Copernicus Knowledge Base - ECMWF Confluence Wiki, https://confluence.ecmwf.int/display/CKB/Description+of+the+CO2+inversion+production+chain, 2024.

410   Chevallier, F., Lloret, Z., Cozic, A., Takache, S., and Remaud, M.: Toward High-Resolution Global Atmospheric Inverse Modeling Using Graphics Accelerators, Geophysical Research Letters, 50, https://doi.org/10.1029/2022GL102135, 2023.

Crippa, M., Guizzardi, D., Pagani, F., Banja, M., Muntean, M., Schaaf E., B., W., Monforti-Ferrario, F., Quadrelli, R., Risquez Martin, A., Taghavi-Moharamli, P., Köykkä, J., Grassi, G., Rossi, S., Brandao De Melo, J., Oom, D., Branco, A., and San-Miguel, E.: EDGAR (Emissions Database for Global Atmospheric Research) Community GHG database, comprising IEA-EDGAR CO_2, EDGAR CH_4, EDGAR

415   N_2O and EDGAR F-gases version 8.0, https://doi.org/doi:10.2760/953322, 2023.

Crisp, D.: Measuring atmospheric carbon dioxide from space with the Orbiting Carbon Observatory-2 (OCO-2), in: Earth Observing Systems XX, edited by Butler, J. J., Xiong, X. J., and Gu, X., vol. 9607, p. 960702, Earth Observing Systems XX, ISBN 9781628417739, ISSN 1996756X, https://doi.org/10.1117/12.2187291, 2015.

Deutscher, N. M., Griffith, D. W., Paton-Walsh, C., Jones, N. B., Velazco, V. A., Wilson, S. R., Macatangay, R. C., Kettlewell, G. C.,

420   Buchholz, R. R., Riggenbach, M. O., Bukosa, B., John, S. S., Walker, B. T., and Naw, H.: TCCON data from Wollongong (AU), Release GGG2020.R0, https://data.caltech.edu/records/ne5d5-49f48, 2023a.

Deutscher, N. M., Griffith, D. W. T., Paton-Walsh, C., Velazco, V. A., Wennberg, P. O., Blavier, J.-F., Washenfelder, R. A., Yavin, Y., Keppel-Aleks, G., Toon, G. C., Jones, N. B., Kettlewell, G. C., Connor, B. J., Macatangay, R. C., Wunch, D., Roehl, C., and Bryant, G. W.: TCCON data from Darwin (AU), Release GGG2020.R0, https://doi.org/10.14291/TCCON.GGG2020.DARWIN01.R0, 2023b.

425   Hachmeister, J.: JonasHach/dlmhelper: Pre-release of v1.0.0, https://doi.org/10.5281/ZENODO.14772372, 2025.

Hachmeister, J., Schneising, O., Buchwitz, M., Burrows, J. P., Notholt, J., and Buschmann, M.: Zonal variability of methane trends derived from satellite data, Atmos. Chem. Phys, 24, 577–595, https://doi.org/10.5194/acp-24-577-2024, 2024.

Iraci, L. T., Podolske, J. R., Roehl, C., Wennberg, P. O., Blavier, J.-F., Allen, N., Wunch, D., and Osterman, G. B.: TCCON data from Edwards (US), Release GGG2020.R0, https://doi.org/10.14291/TCCON.GGG2020.EDWARDS01.R0, 2022.

430 Jacobson, A. R., Schuldt, K. N., Tans, P., Andrews, A., Miller, J. B., Oda, T., Basu, S., Mund, J., Weir, B., Ott, L., Aalto, T., Abshire, J. B., Aikin, K., Aoki, S., Apadula, F., Arnold, S., Baier, B., Bartyzel, J., Beyersdorf, A., Biermann, T., Biraud, S. C., Boenisch, H., Brailsford, G., Brand, W. A., Chen, G., Chen, H., Chmura, L., Clark, S., Cox, A., Cristofanelli, P., Cuevas, E., Curcoll, R., Daube, B., Davis, K. J., De Wekker, S., Della Coletta, J., Delmotte, M., Digangi, E., Digangi, J. P., Giorgio, A., Sarra, D., Dlugokencky, E., Elkins, J. W., Emmenegger, L., Fang, S., Fischer, M. L., Forster, G., Frumau, A., Galkowski, M., Gatti, L. V., Gehrlein, T., Gerbig, C., Gheusi, F.,
435 Gloor, E., Gomez-Trueba, V., Goto, D., Griffis, T., Hammer, S., Hanson, C., Haszpra, L., Hatakka, J., Heimann, M., Heliasz, M., Hensen, A., Hermansen, O., Hintsa, E., Holst, J., Ivakhov, V., Jaffe, D. A., Jordan, A., Joubert, W., Karion, A., Kawa, S. R., Kazan, V., Keeling, R. F., Keronen, P., Kneuer, T., Kolari, P., Komínková, K., Kort, E., Kozlova, E., Krummel, P., Kubistin, D., Labuschagne, C., Lam, D. H. Y., Lan, X., Langenfelds, R. L., Laurent, O., Laurila, T., Lauvaux, T., Lavric, J., Law, B. E., Lee, J., Lee, O. S. M., Lehner, I., Lehtinen, K., Leppert, R., Leskinen, A., Leuenberger, M., Levin, I., Levula, J., Lin, J., Lindauer, M., Loh, Z., Lopez, M., Luijkx, I. T., Lunder, C. R.,
440 Machida, T., Mammarella, I., Manca, G., Manning, A., Manning, A., Marek, M. V., Martin, M. Y., Matsueda, H., Mckain, K., Meijer, H., Meinhardt, F., Merchant, L., Mihalopoulos, N., Miles, N. L., Miller, C. E., Mitchell, L., Mölder, M., Montzka, S., Moore, F., Moossen, H., Morgan, E., Morgui, J.-A., Morimoto, S., Müller-Williams, J., Munger, J. W., Munro, D., Lund Myhre, C., Nakaoka, S.-I., Necki, J., Newman, S., Nichol, S., Niwa, Y., Obersteiner, F., O'doherty, S., Paplawsky, B., Peischl, J., Peltola, O., Piacentino, S., Pichon, J.-M., Pickers, P., Piper, S., Pitt, J., Plass-Dülmer, C., Platt, S. M., Prinzivalli, S., Ramonet, M., Ramos, R., Reyes-Sanchez, E., Richardson,
445 S. J., Riris, H., Rivas, P. P., Ryerson, T., Saito, K., and Sargent, M.: CarbonTracker Documentation CT2022 release, Tech. rep., National Oceanic and Atmospheric Administration, 2023.

Keppel-Aleks, G., Wennberg, P. O., and Schneider, T.: Sources of variations in total column carbon dioxide, Atmos. Chem. Phys, 11, 3581–3593, https://doi.org/10.5194/acp-11-3581-2011, 2011.

Kivi, R. and Heikkinen, P.: Fourier transform spectrometer measurements of column CO2 at Sodankylä, Finland, Geoscientific Instrumenta-
450 tion, Methods and Data Systems, 5, 271–279, https://doi.org/10.5194/GI-5-271-2016,, 2016.

Kivi, R., Heikkinen, P., and Kyra, E.: TCCON data from Sodankyla (FI), Release GGG2020.R0, https://doi.org/10.14291/TCCON.GGG2020.SODANKYLA01.R0, 2022.

Labzovskii, L. D., Kenea, S. T., Lindqvist, H., Kim, J., Li, S., Byun, Y. H., and Goo, T. Y.: Towards robust calculation of interannual CO_2 growth signal from TCCON (Total Carbon Column Observing Network), Remote Sensing, 13, 3868,
455 https://doi.org/10.3390/RS13193868/S1, 2021.

Laine, M.: Introduction to Dynamic Linear Models for Time Series Analysis, pp. 139–156, https://doi.org/10.1007/978-3-030-21718-1_4, 2020.

Lan, X., Tans, P., and Thoning, K.: Trends in CO2 - NOAA Global Monitoring Laboratory, https://gml.noaa.gov/ccgg/trends/global.html, 2025.

460 Laughner, J. L., Toon, G. C., Mendonca, J., Petri, C., Roche, S., Wunch, D., Blavier, J. F., Griffith, D. W., Heikkinen, P., Keeling, R. F., Kiel, M., Kivi, R., Roehl, C. M., Stephens, B. B., Baier, B. C., Chen, H., Choi, Y., Deutscher, N. M., Digangi, J. P., Gross, J., Herkommer, B., Jeseck, P., Laemmel, T., Lan, X., McGee, E., McKain, K., Miller, J., Morino, I., Notholt, J., Ohyama, H., Pollard, D. F., Rettinger, M., Riris, H., Rousogenous, C., Sha, M. K., Shiomi, K., Strong, K., Sussmann, R., Té, Y., Velazco, V. A., Wofsy, S. C., Zhou, M., and Wennberg, P. O.: The Total Carbon Column Observing Network's GGG2020 data version, Earth System Science Data, 16, 2197–2260,
465 https://doi.org/10.5194/ESSD-16-2197-2024, 2024.

Lee, H., Calvin, K., Dasgupta, D., Krinner, G., Mukherji, A., Thorne, P., Trisos, C., Romero, J., Aldunce, P., Barret, K., and Blanco, G.: CLI-MATE CHANGE 2023 Synthesis Report, Sixth Assessment Report of the Intergovernmental Panel on Climate Change, Tech. rep., Inter-

governmental Panel on Climate Change - Core Writing Team m, H. Lee and J. Romero (eds.), Geneva, Switzerland, ISBN 9789291691647, https://doi.org/10.59327/IPCC/AR6-9789291691647, 2023.

470 Lindqvist, H., O'Dell, C. W., Basu, S., Boesch, H., Chevallier, F., Deutscher, N., Feng, L., Fisher, B., Hase, F., Inoue, M., Kivi, R., Morino, I., Palmer, P. I., Parker, R., Schneider, M., Sussmann, R., and Yoshida, Y.: Does GOSAT capture the true seasonal cycle of carbon dioxide?, Atmos. Chem. Phys, 15, 13 023–13 040, https://doi.org/10.5194/acp-15-13023-2015, 2015.

Lucchesi, R.: File Specification for GEOS-5 FP-IT (Forward Processing for Instrument Teams), http://gmao.gsfc.nasa.gov/pubs/office_notes., 2013.

475 Met Office: GitHub - SciTools/cartopy: Cartopy - a cartographic python library with matplotlib support, https://cartopy.readthedocs.io, 2024.

Morino, I., Ohyama, H., Hori, A., and Ikegami, H.: TCCON data from Rikubetsu (JP), Release GGG2020.R0, https://doi.org/10.14291/TCCON.GGG2020.RIKUBETSU01.R0, 2022.

Natural Earth.: Natural Earth » Features - Free vector and raster map data at 1:10m, 1:50m, and 1:110m scales, https://www.naturalearthdata.com/features/, 2025.

480 NOAA: Trends in Atmospheric Carbon Dioxide, Earth System Research Laboratories - Global Monitoring Laboratory, 2024.

Pollard, D. F., Robinson, J., and Shiona, H.: TCCON data from Lauder (NZ), Release GGG2020.R0, https://doi.org/10.14291/TCCON.GGG2020.LAUDER03.R0, 2022.

Reuter, M., Buchwitz, M., Schneising, O., Noël, S., Bovensmann, H., Burrows, J. P., Boesch, H., Di Noia, A., Anand, J., Parker, R. J., Somkuti, P., Wu, L., Hasekamp, O. P., Aben, I., Kuze, A., Suto, H., Shiomi, K., Yoshida, Y., Morino, I., Crisp, D., O'Dell, C. W., Notholt, 485 J., Petri, C., Warneke, T., Velazco, V. A., Deutscher, N. M., Griffith, D. W., Kivi, R., Pollard, D. F., Hase, F., Sussmann, R., Té, Y. V., Strong, K., Roche, S., Sha, M. K., De Mazière, M., Feist, D. G., Iraci, L. T., Roehl, C. M., Retscher, C., and Schepers, D.: Ensemble-based satellite-derived carbon dioxide and methane column-averaged dry-air mole fraction data sets (2003-2018) for carbon and climate applications, Atmos. Meas. Tech, 13, 789–819, https://doi.org/10.5194/AMT-13-789-2020, 2020.

Shiomi, K., Kawakami, S., Ohyama, H., Arai, K., Okumura, H., Ikegami, H., and Usami, M.: TCCON data from Saga (JP), Release 490 GGG2020.R0, https://doi.org/10.14291/TCCON.GGG2020.SAGA01.R0, 2022.

Stephens, B. B., Brailsford, G. W., Gomez, A. J., Riedel, K., Mikaloff Fletcher, S. E., Nichol, S., and Manning, M.: Analysis of a 39-year continuous atmospheric CO_2 record from Baring Head, New Zealand, Biogeosciences, 10, 2683–2697, https://doi.org/10.5194/BG-10-2683-2013, 2013.

Strong, K., Roche, S., Franklin, J. E., Mendonca, J., Lutsch, E., Weaver, D., Fogal, P. F., Drummond, J. R., Batchelor, R., Lindenmaier, R., 495 and McGee, E.: TCCON data from Eureka (CA), Release GGG2020.R0, https://doi.org/10.14291/TCCON.GGG2020.EUREKA01.R0, 2022.

Sussmann, R. and Rettinger, M.: Can We Measure a COVID-19-Related Slowdown in Atmospheric CO_2 Growth? Sensitivity of Total Carbon Column Observations, Remote Sensing 2020, Vol. 12, Page 2387, 12, 2387, https://doi.org/10.3390/RS12152387, 2020.

Sussmann, R. and Rettinger, M.: TCCON data from Garmisch (DE), Release GGG2020.R1, 500 https://doi.org/10.14291/TCCON.GGG2020.GARMISCH01.R1, 2025.

TCCON Team: 2020 Total Carbon Column Observing Network Data Release (Version GGG2020), https://doi.org/https://doi.org/10.14291/TCCON.GGG2020, 2020.

Thoning, K., Crotwell, A., and Mund, J.: Atmospheric Carbon Dioxide Dry Air Mole Fractions from continuous measurements at Mauna Loa, Hawaii, Barrow, Alaska, American Samoa and South Pole, 1973-present. Version 2024-06-07, 505 https://doi.org/https://doi.org/10.15138/yaf1-bk21, 2024.

UNFCC: Paris Agreement, Tech. rep., United Nations Framework Convention on Climate Change, 2015.

Wennberg, P. O., Roehl, C. M., Wunch, D., Toon, G. C., Blavier, J.-F., Washenfelder, R., Keppel-Aleks, G., and Allen, N. T.: TCCON data from Park Falls (US), Release GGG2020.R1, https://doi.org/10.14291/TCCON.GGG2020.PARKFALLS01.R1, 2022a.

Wennberg, P. O., Wunch, D., Roehl, C. M., Blavier, J.-F., Toon, G. C., and Allen, N. T.: TCCON data from Lamont (US), Release
510   GGG2020.R0, https://doi.org/10.14291/TCCON.GGG2020.LAMONT01.R0, 2022b.

Wunch, D., Toon, G. C., Wennberg, P. O., Wofsy, S. C., Stephens, B. B., Fischer, M. L., Uchino, O., Abshire, J. B., Bernath, P., Biraud, S. C., Blavier, J.-F. L., Boone, C., Bowman, K. P., Browell, E. V., Campos, T., Connor, B. J., Daube, B. C., Deutscher, N. M., Diao, M., Elkins, J. W., Gerbig, C., Gottlieb, E., Griffith, D. W. T., Hurst, D. F., Jiménez, R., Keppel-Aleks, G., Kort, E. A., Macatangay, R., Machida, T., Matsueda, H., Moore, F., Morino, I., Park, S., Robinson, J., Roehl, C. M., Sawa, Y., Sherlock, V., Sweeney, C., Tanaka,
515   T., and Zondlo, M. A.: Calibration of the Total Carbon Column Observing Network using aircraft profile data, Atmos. Meas. Tech, 3, 1351–1362, https://doi.org/10.5194/amt-3-1351-2010, 2010.

Yokota, T., Yoshida, Y., Eguchi, N., Ota, Y., Tanaka, T., Watanabe, H., and Maksyutov, S.: Global concentrations of CO_2 and CH_4 retrieved from GOSAT: First preliminary results, Scientific Online Letters on the Atmosphere, 5, 160–163, https://doi.org/10.2151/sola.2009-041, 2009.

520   Zhang, Y., Dannenberg, M. P., Hwang, T., and Song, C.: El Niño-Southern Oscillation-Induced Variability of Terrestrial Gross Primary Production During the Satellite Era, Journal of Geophysical Research: Biogeosciences, 124, 2419–2431, https://doi.org/10.1029/2019JG005117;CTYPE:STRING:JOURNAL, 2019.